Available online at www.sciencedirect.com
ScienceDirect
Journal of Solid State Chemistry 180 (2007) 2808–2815
JOURNAL OF SOLID STATE CHEMISTRY
www.elsevier.com/locate/jssc

Physicochemical compatibility of $SrCeO_3$ with potential SOFC cathodes

J. Tolchard, T. Grande*

Department of Materials Science and Engineering, Norwegian University of Science and Technology, N-7491 Trondheim, Norway

Received 30 April 2007; received in revised form 9 August 2007; accepted 9 August 2007
Available online 23 August 2007

Abstract

The chemical and physical compatibility of $SrCeO_3$ is investigated with respect to $LaMO_3$ (M = Mn, Fe, Co) and $La_{2-x}Sr_xNiO_4$ ($x = 0$, 0.8), via the reaction of fine-grained powder compacts and solid-state diffusion couples. Compositions were chosen so as to give predictive insight into possible candidate materials for all-oxide electrochemical devices. Results show the primary reaction in these systems to be the dissolution of SrO from $SrCeO_3$ into the $LaMO_3$/$La_{2-x}Sr_xNiO_4$, and corresponding formation of La-doped CeO_2. Reaction kinetics are observed to be relatively fast, with element profiles suggesting the diffusion of Sr^{2+} in ceria to be surprisingly rapid. It is demonstrated that perovskite starting materials represent poor candidates for use with $SrCeO_3$, reacting completely to form Ruddlesden-Popper/K_2NiF_4 type oxides. Reaction with La_2NiO_4 is less pronounced, and formation of secondary phases suppressed for the composition $La_{1.2}Sr_{0.8}NiO_4$. It is thus concluded that Ruddlesden-Popper type oxides represent good candidate materials for use with a $SrCeO_3$-based electrolytes when doped with appropriate levels of Sr.

Keywords: SOFC; Electrode; Perovskite; $SrCeO_3$; K_2NiF_4; Materials compatibility; Diffusion couple

1. Introduction

Proton conducting oxides have attracted considerable recent attention owing to their potential for use in a wide range of electrochemical devices, particularly the technologies which underpin the hydrogen economy; hydrogen separators, steam electrolysers and fuel cells [1–6]. For these applications protonic systems are particularly attractive as they avoid the problems associated with the fuel–product mixing that occurs in oxide ion conducting systems.

Current state of the art in ceramic proton conductors are the barium and strontium cerate families [7,8]. These exhibit a distorted perovskite structure [9], and high levels of proton conductivity are achievable via the replacement of Ce^{4+} with an acceptor dopant such as Y^{3+}, Nd^{3+} Yb^{3+} or Gd^{3+} [10–14]. The commercial application of these materials has been hindered however, by the instability of both Sr and Ba families with respect to their alkaline earth carbonates [15–17], and by the technical difficulty of creating fully dense ceramics with good mechanical properties [18]. A further challenge exists in the pairing of these materials with appropriate electrodes. Typically a porous electrode of a noble metal has been used [5,10]. However, these are expensive and so there is some interest in the development of less costly solutions. Ideally a less expensive oxide ceramic would be used which exhibits combined fast protonic–electronic conductivity, but to date there are no oxides which fulfil these requirements. Possible alternatives exist in the use of a Ni-electrolyte cermet [19] under reducing conditions (i.e. fuel cell anode) and a mixed oxide ion/electronic conductor for oxidising conditions (i.e. fuel cell cathode) [10,13,20]. The use of a mixed electronic/oxide ion conductor greatly broadens the choice of potential electrodes, with the additional benefit that a good understanding of the synthesis, processing and chemistry already exists for many of the candidate materials.

With this in mind, we have investigated the chemical compatibility of the fast protonic conductor $SrCeO_3$ with a number of well-known mixed oxide-ion/electronic conducting oxides. The systems chosen ($LaCoO_3$, $LaMnO_3$, $LaFeO_3$ and $La_{2-x}Sr_xNiO_4$) are representative of current

*Corresponding author. Fax: +47 73 59 08 60.
E-mail address: tor.grande@material.ntnu.no (T. Grande).

0022-4596/$ - see front matter © 2007 Elsevier Inc. All rights reserved.
doi:10.1016/j.jssc.2007.08.004

materials and provide a solid basis for prediction of other likely candidates.

2. Experimental

Powders of $SrCeO_3$, $LaMnO_3$, $LaFeO_3$, $LaCoO_3$ and $La_{2-x}Sr_xNiO_4$ ($x = 0$, 0.8) were synthesised via spray pyrolysis of appropriate solutions of metal nitrates. A complexing agent, ethylenediaminetetraacetic acid (EDTA), was used to assist dissolution and homogeneous reaction during pyrolysis. The as-prepared powders were then calcined in air to remove residual nitrates/organics, and ball milled in isopropanol for 6–8 h using 5 mm zirconia media. For the $La_{2-x}Sr_xNiO_4$ compositions a calcination temperature of 800 °C was used, whilst $LaMO_3$ phases and $SrCeO_3$ were calcined at the slightly higher temperature of 900 °C. For all phases, the final product consisted of a finely divided, sub micron powder. Analysis via X-ray diffraction confirmed phase purity in all cases.

Phase compatibility of $SrCeO_3$ with the parent electrode compositions was investigated via two routes:

1. 1:1 mixtures (by mass) of $SrCeO_3$ with each of $LaMO_3$ (M = Mn, Fe, Co) and La_2NiO_4 were uniaxially pressed at 90 MPa and fired at 1150 °C for 36 and 72 h in air.
2. $SrCeO_3$ powder was pressed into tablet form at 80 MPa and fired at 1400 °C to produce dense sintered compacts. These were then polished with fine abrasives down to a size of 1 μm and a slurry of $LaMO_3$ (M = Mn, Fe, Co) or $La_{2-x}Sr_xNiO_4$ ($x = 0$ and 0.8) hand coated onto the polished surface to form a diffusion couple. As reaction kinetics are generally slower in diffusion couple geometry, a higher temperature of 1300 °C and a firing time of 48 h were employed.

Phase formation in the heat-treated powder samples was analysed using a Bruker D8 Advance powder diffractometer (Cu$K\alpha$ radiation, Våntec detector). Phases were identified via the Powder Diffraction File database [21], and confirmed via profile fitting with the Topas 2.1 software suite [22]. The microstructure and composition of both powder compacts and diffusion couples was studied using an Hitachi N-3400 Scanning Electron Microscope (SEM) equipped with an Oxford Instruments INCA X-sight (model 7021) Energy Dispersive X-ray Spectrometer (EDS) with a resolution of 133 eV at 5.9 keV. Samples for SEM/EDS analysis were mounted in epoxy resin, polished with fine abrasives (down to 1 μm) and coated with carbon. Sample composition was analysed via both spot analyses (1 μm^2) and collection of X-ray element maps. Composition line profiles were calculated from the element maps using a spot size in the region 9–16 μm^2. All EDS analysis was performed using the INCA analysis suite, calibrated relative to a Co standard. The estimated error in measured cation compositions is $<5\%$.

3. Results

3.1. Solid-state reaction—microfine powders

Following initial firing for 36 h at 1150 °C powder compacts of $SrCeO_3$ with $LaMO_3$ (M = Mn and Co) showed strong reaction, with complete reaction of $SrCeO_3$ to form product phases identified as the K_2NiF_4 type materials $(La,Sr)_2MO_4$ and a CeO_2-type phase. Small quantities of the starting perovskite were also present. The $SrCeO_3/La_2NiO_4$ system showed similar, but more limited, reaction of $SrCeO_3$, and a concurrent reduction in the La_2NiO_4 unit cell volume. In each case, broad diffraction peaks for the product phases indicated that full equilibrium was not attained so a further firing step of 36 h was applied. Diffractograms obtained after this step showed improvement in the homogeneity of the product phases, and no additional reactions. These are presented in Fig. 1A, with the equilibrium product phases labelled. According to the Gibbs phase rule ($ph+f = c+2$) a system with 5 components (Ce, La, M, Sr and O) at a given temperature and pressure can exhibit a maximum of 5 phases at equilibrium (4 solid phases + $O_{2(g)}$). At constant pO_2 the number of condensed phases reduces to 3, in accord with these observations.

Similar reactivity was observed for M = Fe, but with the product phases being a mixture of $(La,Sr)_2FeO_4$ and a Ruddlesden-Popper (R-P) type material. The presence of 4 condensed phases (perovskite, ceria, $(La,Sr)_2FeO_4$, and R-P type) indicates non-equilibrium, and so further firing steps were performed. Equilibrium in the system was attained after 120 h firing, the equilibrium phases being residual $LaFeO_3$, ceria, and the R-P material (Fig. 1B). Two R-P systems are known to exist in this system, $La_{3-x}Sr_xFe_2O_{7-\delta}$ ($1 \leqslant x < 1.15$ and $2.6 < x \leqslant 3$) and $LaSr_3Fe_3O_{10-\delta}$ [23–25]. However, the formation of $La_{3-x}Sr_xFe_2O_{7-\delta}$ ($1 \leqslant x < 1.15$) requires reaction of considerably more $LaFeO_3$ than $SrCeO_3$, and the experimental results show residual $LaFeO_3$, not $SrCeO_3$. The production of either of the Sr-rich systems, $La_{3-x}Sr_xFe_2O_{7-\delta}$ ($2.6 < x \leqslant 3$) or $LaSr_3Fe_3O_{10-\delta}$, agrees well with the experimental results. However, strong peak overlap between the observed phases in the 31–35° 2θ range obscures the 100% peak of the remaining perovskite, and inhibits the quantitative phase analysis necessary to conclusively ascertain which phase is formed. We can thus propose the following simplified reaction schemes:

For reaction of $LaMO_3$ (M = Co, Mn):

$$LaMO_3 + (1+y)SrCeO_3 + \frac{y}{4}O_{2(g)} \rightarrow La_{1-y}Sr_{1+y}MO_4 + (1+2y)La_{(y/1+2y)}Ce_{(1+y/1+2y)}O_{2-(y/2+4y)}.$$

For reaction of $LaFeO_3$ one of the following two reactions is proposed:

$$LaFeO_3 + \left(\frac{1+y}{2}\right)SrCeO_3 + \frac{y}{8}O_{2(g)} \rightarrow \frac{1}{2}La_{2-y}Sr_{1+y}Fe_2O_7 + \left(\frac{1+2y}{2}\right)La_{(y/1+2y)}Ce_{(1+y/1+2y)}O_{2-(y/2+4y)}.$$

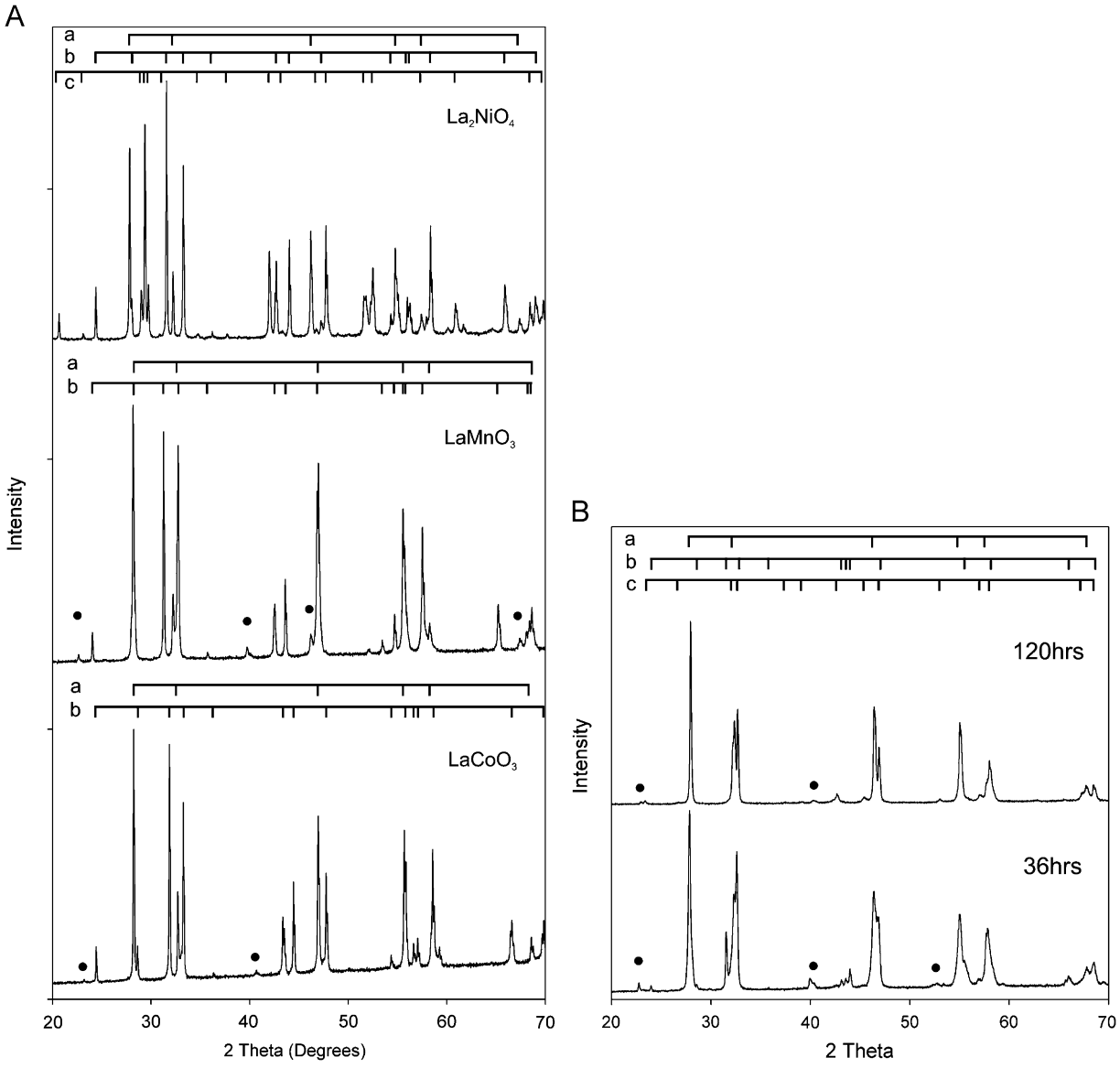

Fig. 1. (A) X-ray diffractograms of powder composites of $SrCeO_3$ with $LaCoO_3$, $LaMnO_3$ and La_2NiO_4. Taken after 72 h firing at 1150 °C. Peak positions are shown for the equilibrium phases: (a) doped-CeO_2, (b) $(La,Sr)_2MO_4$ and (c) $SrCeO_3$. Residual traces of $LaMO_3$ perovskite are shown with a solid circle. (B) X-ray diffractograms of $SrCeO_3/LaFeO_3$ powder composites taken after 36 and 120 h firing at 1150 °C. Peak positions are shown for the product phases: (a) doped-CeO_2, (b) $(La,Sr)_2FeO_4$ and (c) $La_{3-x}Sr_xFe_2O_7$. Residual traces of $LaFeO_3$ perovskite are shown with a solid circle.

or

$$LaFeO_3 + SrCeO_3 + \frac{1}{6}O_{2(g)} \rightarrow \frac{1}{3}LaSr_3Fe_3O_{10} + \frac{5}{3}La_{2/5}Ce_{3/5}O_{9/5}.$$

Reaction with La_2NiO_4 is more limited, reflecting compatibility of the $SrCeO_3$ with K_2NiF_4 type stoichiometry. Here stability is achieved without exceeding the Sr solubility limit:

$$La_2NiO_4 + ySrCeO_3 + \frac{y}{4}O_{2(g)} \rightarrow La_{2-y}Sr_yNiO_4 + 2yLa_{1/2}Ce_{1/2}O_{7/4}.$$

An enlarged unit cell for the ceria phases indicates a significant level of La doping, and comparison of our unit cell data with that of Morris et al. [26] for $La_xCe_{1-x}O_{2-x/2}$ (Fig. 2), gives approximate values of $x = 0.18$, 0.22 and 0.34 for M = Co, Mn and Fe systems, respectively. Given the low quantity of residual perovskite evidenced by diffraction, the relatively high value of x for M = Fe tends to support formation of $LaSr_3Fe_3O_{10}$ over $La_{2-y}Sr_{1+y}Fe_2O_7$. For the $SrCeO_3/La_2NiO_4$ composite, the higher value of $x = 0.43$ is in good accord with the predicted value. It should be noted that due its low solubility ($x < 0.09$) [27] and the similar ionic radii of La^{3+} and Sr^{2+} [28], dissolution of Sr in ceria is ignored in these schemes. Accurate estimates of composition for the $(La,Sr)_2MO_4$ phases were not possible for the M = Co and M = Mn systems due to a lack of agreement in previously reported data [29–31]. For the M = Ni system however, an approximate value of $x = 0.6$ was

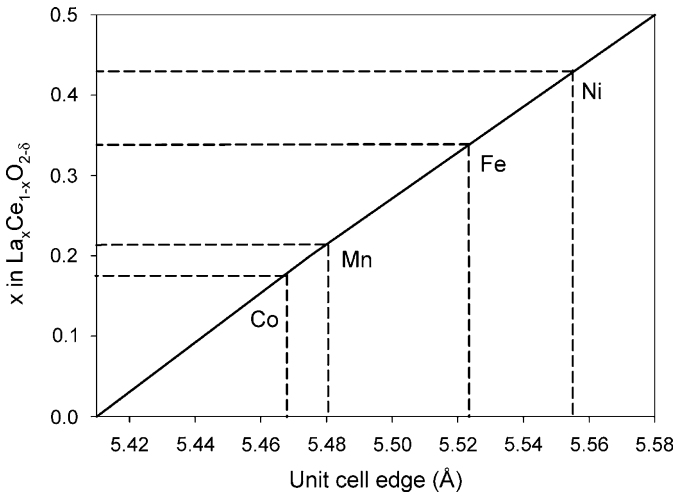

Fig. 2. Measured unit cell edges vs. composition for $La_xCe_{1-x}O_{2-x/2}$. La doping level (x) is estimated from diffraction data (broken lines) using the values of Morris et al. (solid line) as a reference.

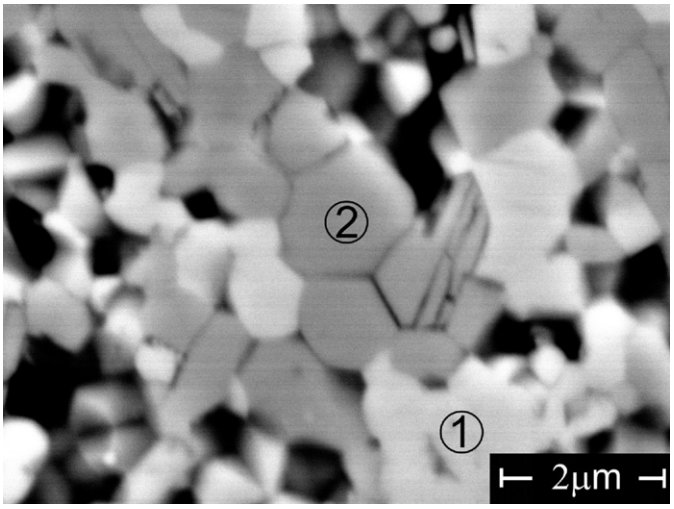

Fig. 3. Backscattering electron micrograph image of a $SrCeO_3/LaCoO_3$ powder composite after 36 h firing at 1150 °C. Compositions at points 1 and 2 are discussed in the main text.

obtained from comparison of our data with that of Heaney et al. [32].

Fig. 3 shows the microstructure of the $SrCeO_3/LaCoO_3$ compact following 36 h firing, and is representative of all systems. In all cases, the powder compacts showed poor physical structure, with large quantities of material "pulled out" during the polishing process. This can be clearly seen in Fig. 3, along with a high degree of inter-grain cracking. This poor structure arises from the large structural changes which accompany the formation of doped CeO_2 and (for the $LaMO_3$ phases) the R-P phases. Further stresses on cooling arise from the differing thermal expansion coefficients.

EDS composition analysis confirmed the phases found by diffraction. These are labelled in Fig. 3 for the $SrCeO_3/LaCoO_3$ composite:

Phase 1 is the doped-CeO_2 material, best described as $La_xSr_yCe_{1-x-y}O_{2-\delta}$. In line with previous reports [27] the Sr content of this phase was found to be much lower than the La content. A large range of measured x compositions in each sample ($0.07 < x < 0.2$ in the $SrCeO_3/LaCoO_3$ composite shown) confirms the origin of the broad diffraction peaks.

Phase 2 is the product $(La,Sr)_2MO_4$ phase. Again, some variation in composition is seen across the sample, but much less than for the doped ceria phase. Approximate values of $x = 1.1$, 1.2 and 1.4 (in $La_{2-x}Sr_xMO_4$) were found for $M =$ Co, Fe and Mn, respectively. For $M =$ Fe only regions of $(La,Sr)_2FeO_4$ were identified, probably due to only small domains of the R-P phase being present at this stage of firing.

3.2. Solid-state reaction–diffusion couples

Backscattered electron images for the diffusion couples of $SrCeO_3$ with $LaMO_3$ ($M =$ Mn, Co, Fe) and La_2NiO_4 are shown in Figs. 4–7. As formation of the Sr substituted La_2MO_4/R-P phases observed by powder diffraction implies coexistence of these phases with $SrCeO_3$ an additional diffusion couple was tested with the composition $La_{1.2}Sr_{0.8}NiO_4$. This is shown in Fig. 8. Compositional analysis was performed at specific points through each couple using EDS. These are labelled 1–5, with the corresponding compositions presented in Table 1. Additionally, X-ray element maps were collected for a section of each couple, though only results for $LaMnO_3$ and La_2NiO_4 are presented as these are representative of the other systems.

For all systems the results of the powder compacts were broadly confirmed, with formation of doped CeO_2 and dissolution of Sr into the starting $LaMO_3/La_2NiO_4$. The higher firing temperature results in small differences in the Sr content for $M =$ Ni and Co relative to the powder samples, and the slower kinetics of the diffusion couple geometry stabilises the $(La,Sr)_2FeO_4$ phase. An A:B ratio of 8:5 is calculated for the $M =$ Mn couple, but as this composition is not observed in phase diagrams [33] of the system, a nominal $(La,Sr)_2MnO_4$ composition is assumed. For the $La_{1.2}Sr_{0.8}NiO_4$ couple no secondary phase formation was observed, confirming the improved stability of the Sr doped composition.

As the original heterophase interface can be clearly identified from the sample microstructure, the order of the product layers indicates that SrO is lost from $SrCeO_3$ and diffuses into the $LaMO_3/La_2NiO_4$: Grain growth is evident in the layered microstructure of the transition metal materials, particularly for the perovskite starting compositions, and the $CeO_2/SrCeO_3$ interface is seen to move into the bulk of the initial $SrCeO_3$ dense compact. This is shown schematically in Fig. 9. EDS composition analysis shows a clear boundary between the $SrCeO_3$ and CeO_2 phases. In accord with previous studies, no Sr depletion is seen in the $SrCeO_3$ close to the phase

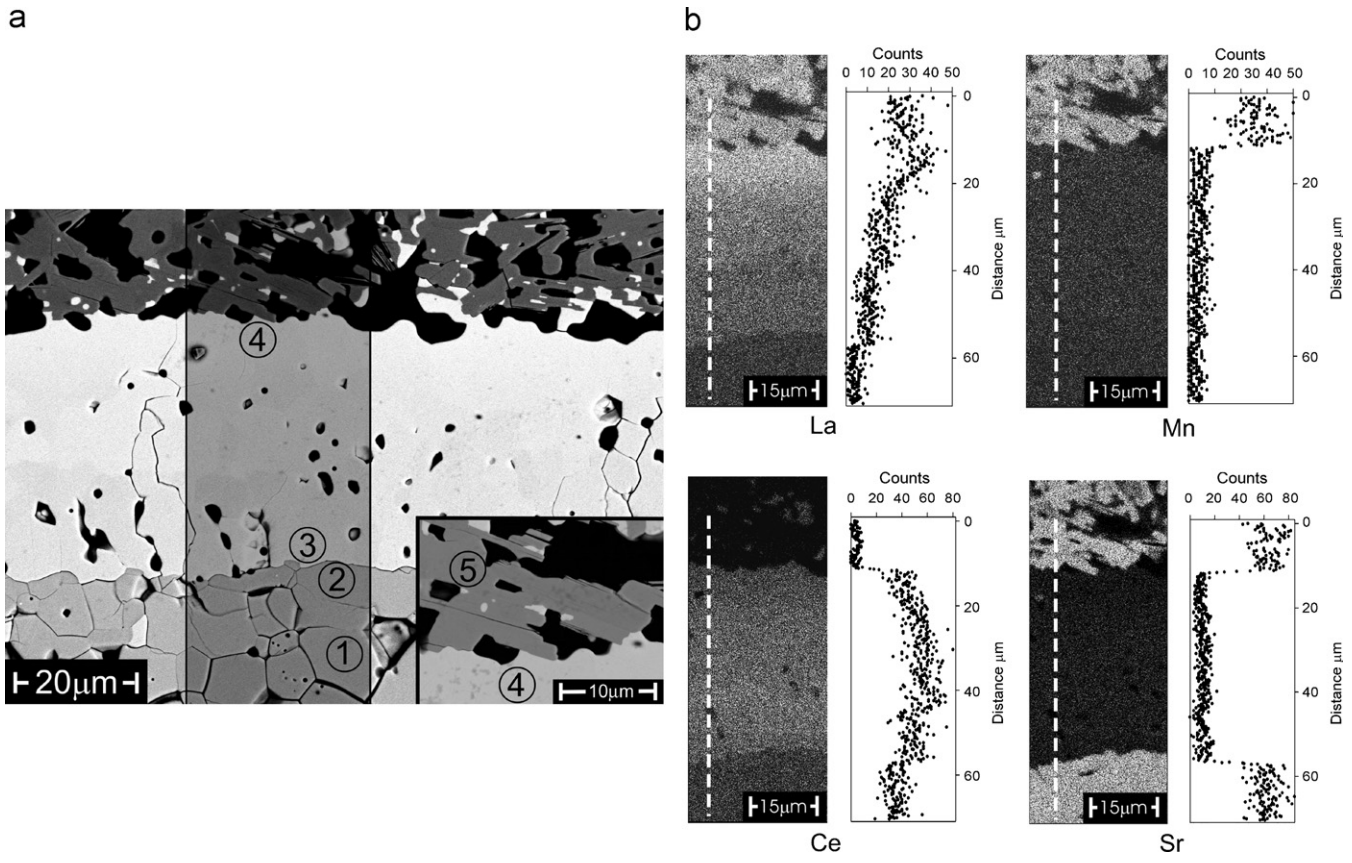

Fig. 4. (a) Backscattering electron micrograph of the $SrCeO_3/LaMnO_3$ diffusion couple after 48 h firing at 1300 °C. Inset is a close-up of the $LaMnO_3/CeO_2$ interface. Numbers correspond to EDS compositions presented in Table 1. (b) X-ray maps collected across the shaded area shown in (a). Cation concentration profiles taken along the dotted line shown are given.

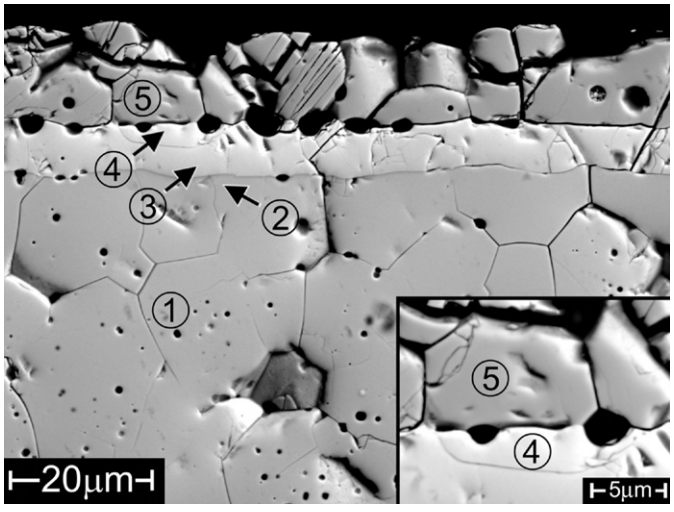

Fig. 5. Backscattering electron micrograph of the $SrCeO_3/LaCoO_3$ diffusion couple after 48 h firing at 1300 °C. Inset is a close-up of the $La_{2-x}Sr_xCoO_4/CeO_2$ interface. Numbers correspond to EDS compositions presented in Table 1.

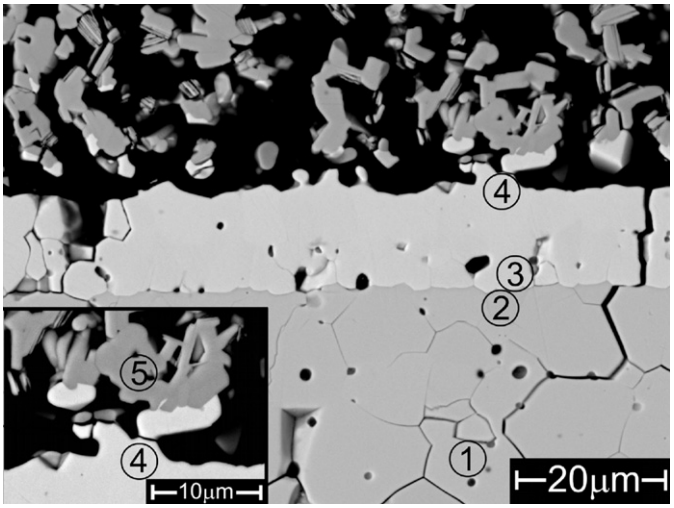

Fig. 6. Backscattering electron micrograph of the $SrCeO_3/LaFeO_3$ diffusion couple after 48 h firing at 1300 °C. Inset is a close-up of the $La_{2-x}Sr_xFeO_4/CeO_2$ interface. Numbers correspond to EDS compositions presented in Table 1.

boundary and solubility of Sr into ceria is low [27]. In contrast, both spot analyses and element maps show a clear La composition gradient across the $La_xCe_{1-x}O_{2-\delta}$ layer. Some solubility of Ce into both the $La_{1.2}Sr_{0.8}NiO_4$ and $(La,Sr)_2CoO_4$ phases was also seen, as has been reported previously [34].

Both the doped CeO_2 and $SrCeO_3$ show similar large grain structure, which arises from grain growth in the

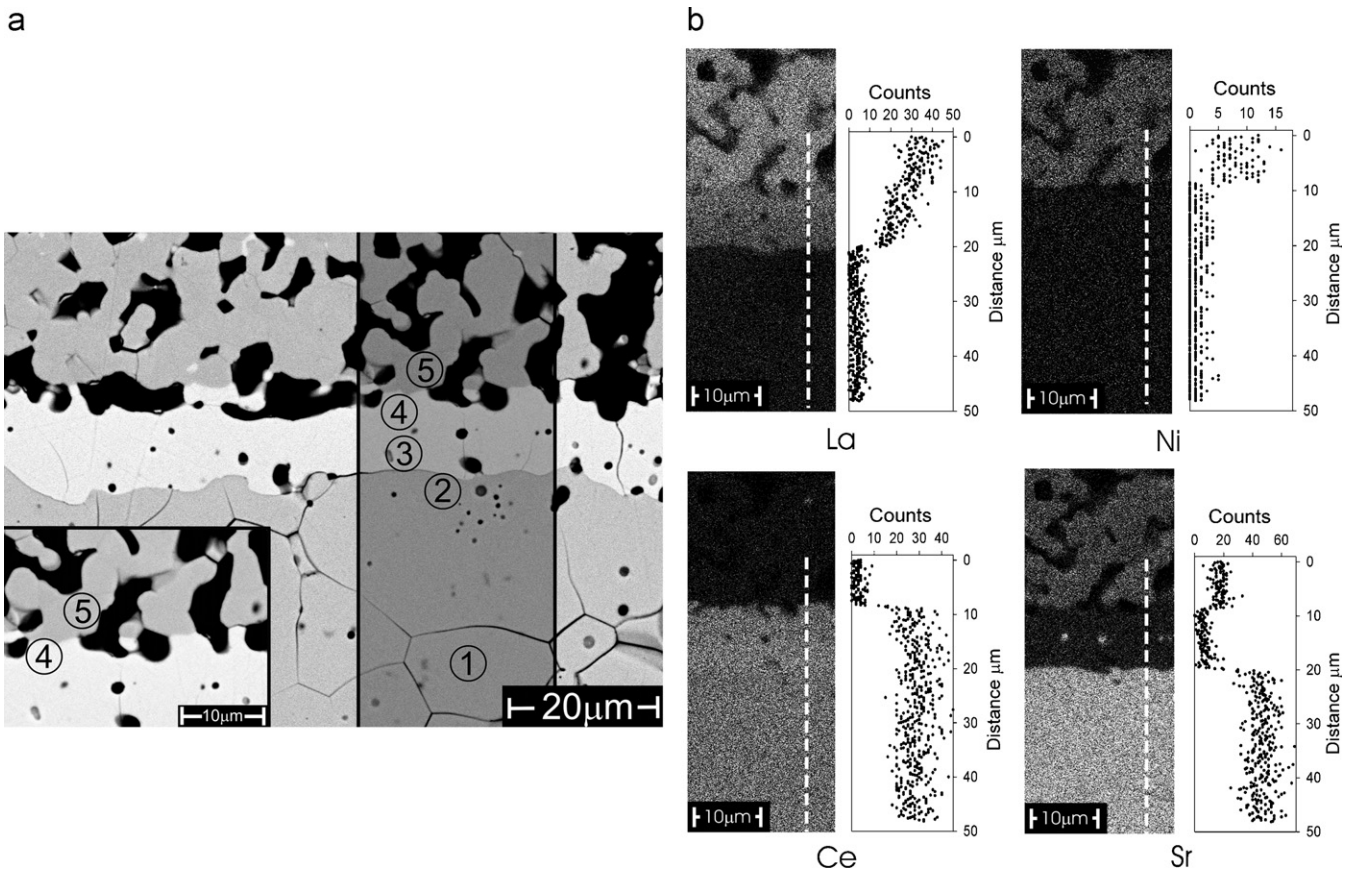

Fig. 7. (a) Backscattering electron micrograph of the $SrCeO_3/La_2NiO_4$ diffusion couple after 48 h firing at 1300 °C. Inset is a close-up of the $La_{2-x}Sr_xNiO_4/CeO_2$ interface. Numbers correspond to EDS compositions presented in Table 1. (b) X-ray maps collected across the shaded area shown in (a). Cation concentration profiles taken along the dotted line shown are given.

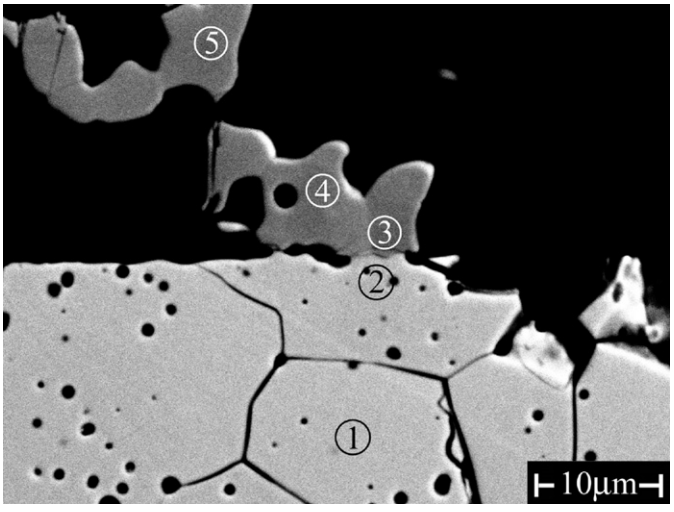

Fig. 8. Backscattering electron micrograph of the $SrCeO_3/La_{1.2}Sr_{0.8}NiO_4$ diffusion couple after 48 h firing at 1300 °C. Numbers correspond to EDS compositions presented in Table 1.

$SrCeO_3$ phase early in the firing regime. However, the $SrCeO_3$ layer demonstrates a very high degree of inter-grain cracking, which extends throughout the $SrCeO_3$ compact, and is not limited to the interface region with CeO_2. The more intact CeO_2 layer indicates that the fractures occur on cooling and are unrelated to any volume changes or chemical expansion effects which occur during the $SrCeO_3$ to CeO_2 transition or the subsequent dissolution of La into ceria. As CeO_2 and $SrCeO_3$ show similar bulk thermal expansion coefficients, the high level of cracking in $SrCeO_3$ likely arises from the combination of large grains and anisotropic contraction on cooling, which introduces local grain boundary stresses. The CeO_2 layer, whilst sharing similar grain structure, is cubic in symmetry and the associated isotropic contraction on cooling limits inter-grain stresses. Compatibility at the $(La,Sr)_2MO_4/CeO_2$ interface seems good for all samples, the volume change of the perovskite to $(La,Sr)_2MO_4$ transition being accommodated by way of grain growth.

4. Discussion

The thermochemical properties of the alkaline earth cerates have been thoroughly addressed by several studies due to their generally poor stability under typical fuel cell operating conditions. In addition to being unstable in CO_2-containing and humid atmospheres, they are also known to be poorly stable with respect to their binary oxides. This is reflected in the Goldschmidt tolerance (t)

Table 1
Phases calculated via EDS analysis of the diffusion couples presented in Figs. 4–8

Position	Diffusion couple				
	$SrCeO_3/LaMnO_3$	$SrCeO_3/LaCoO_3$	$SrCeO_3/LaFeO_3$	$SrCeO_3/La_2NiO_4$	$SrCeO_3/La_{1.2}Sr_{0.8}NiO_4$
1	$Sr_{1.0}Ce_{1.0}O_{3-\delta}$	$La_{0.1}Sr_{0.9}Ce_{1.0}O_{3-\delta}$	$Sr_{1.0}Ce_{1.0}O_{3-\delta}$	$Sr_{1.0}Ce_{1.0}O_{3-\delta}$	$Sr_{1.0}Ce_{1.0}O_{3-\delta}$
2	$Sr_{1.0}Ce_{1.0}O_{3-\delta}$	$Sr_{1.0}Ce_{1.0}O_{3-\delta}$	$Sr_{1.0}Ce_{1.0}O_{3-\delta}$	$La_{0.1}Sr_{0.9}Ce_{1.0}O_{3-\delta}$	$Sr_{1.0}Ce_{1.0}O_{3-\delta}$
3	$La_{0.1}Sr_{0.1}Ce_{0.8}O_{2-\delta}$	$La_{0.2}Sr_{0.1}Ce_{0.7}O_{2-\delta}$	$La_{0.1}Sr_{0.1}Ce_{0.8}O_{2-\delta}$	$La_{0.3}Sr_{0.1}Ce_{0.6}O_{2-\delta}$	$La_{1.0}Ce_{0.2}Sr_{0.9}Ni_{0.9}O_{4+\delta}$
4	$La_{0.4}Ce_{0.6}O_{2-\delta}$	$La_{0.2}Sr_{0.1}Ce_{0.7}O_{2-\delta}$	$La_{0.2}Sr_{0.1}Ce_{0.7}O_{2-\delta}$	$La_{0.5}Ce_{0.5}O_{2-\delta}$	$La_{1.0}Ce_{0.2}Sr_{0.8}Ni_{1.0}O_{4+\delta}$
5	$La_{3.4}Sr_{4.6}Mn_{5.0}O_{17\pm\delta}$	$La_{0.8}Ce_{0.2}Sr_{1.0}Co_{0.9}O_{4+\delta}$	$La_{0.9}Sr_{1.1}Fe_{0.9}O_{4+\delta}$	$La_{1.6}Sr_{0.4}Ni_{0.9}O_{4+\delta}$	$La_{1.2}Ce_{0.1}Sr_{0.8}Ni_{0.9}O_{4+\delta}$

Nominal oxygen compositions are given for each phase, based on the experimentally obtained cation ratios. Position numbers correspond to those presented in Figs. 4–8.

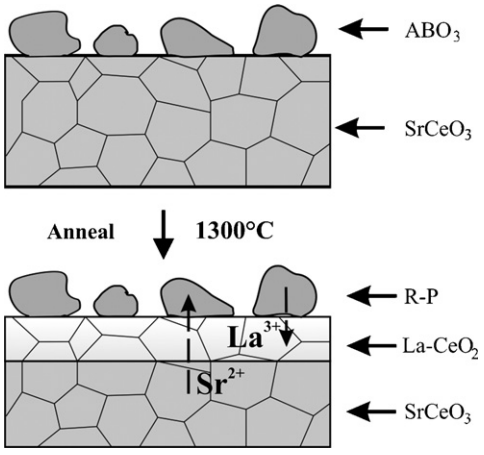

Fig. 9. Schematic of the diffusion couples before (top) and after (bottom) firing.

factors, as enthalpies of formation become less exothermic with decreasing t-values [35]. $SrCeO_3$ is particularly unstable in this respect, with $t = 0.88$ and a reported $\Delta H_f = \sim -5\,kJmol^{-1}$ [36,37] for the reaction:

$$SrO + CeO_2 \rightarrow SrCeO_3.$$

The consequence of this is a high chemical activity of SrO, which causes $LaMO_3$ compositions to be unstable with respect to more Sr-rich R-P phases. The observed product phases, and the improved stability of $La_{2-x}Sr_xNiO_4$ towards $SrCeO_3$, suggest that full coexistence should be achieved via an appropriately doped K_2NiF_4/R-P type phase. The required level of Sr doping in these is expected to vary according to the oxidation chemistry of the transition metal, but relatively high Sr doping levels are anticipated in all cases. We note that several studies have investigated the electrode properties of the $(La,Sr)_2MO_4$ type systems [38–42], and even at the high Sr contents expected for coexistence with $SrCeO_3$, these systems show considerable promise as air electrodes. For the $M = Fe$ systems, the metastability of the $(La,Sr)_2FeO_4$ systems [25] obviously favours use of higher R-P phases, for which little electrode testing has been performed.

Considering the reactivity of $LaMO_3$ systems with other candidate fuel cell electrolytes compatibility with $SrCeO_3$ systems is particularly poor. Perovskite $LaMO_3$ electrodes show good stability with ceria [43], and whilst reaction with LSGM tends to be limited, considerable interdiffusion is known to occur due to solid solubility between the components [44,45]. The YSZ and $BaZrO_3$ systems both undergo reaction with $LaMO_3$, forming the pyrochlore $La_2Zr_2O_7$ at the interface which then acts as a diffusion barrier [46,47]. It is interesting that the driving force in the second of these is similar to that observed here—activity of the alkaline earth metal towards the $LaMO_3$ electrode candidate. However, compatibility is much better for the alkaline earth zirconates, with perovskite stoichiometry preserved after reaction of the electrode candidate. This would imply improved stability of the $AZr_{1-x}Ce_xO_3$ solid solutions [48] over $ACeO_3$.

The kinetics of reaction in the zirconate systems are also much slower than that seen here, reaction being inhibited by slow cation diffusion in the pyrochlore phase [47]. The short timescales for reaction in the present systems, and the homogeneous product phases point to fast bulk cation diffusion. The complete conversion of $LaMO_3$ to $(La,Sr)_2MO_4$ limits mechanistic insight, but relatively fast transport of La and Sr in both materials, as well as through the ceria layer, is implied. Unfortunately solid-state cation diffusion in these systems is under-investigated, so there is insufficient data to allow comparison of rates and mechanisms of Sr and La diffusion in the ceria, perovskite and R-P systems. However, the composition gradient of La in the ceria layer suggests that dissolution of La into CeO_2 may be the rate limiting process in the reactions observed.

Thermomechanical compatibility of the $(La,Sr)_2MO_4$ phases with alkaline earth cerates is also anticipated to be good: Linear thermal expansion coefficients (TECs) of 11.1×10^{-6} and 11.2×10^{-6}, for $SrCeO_3$ and $BaCeO_3$, respectively [49], compare well with values in the range $11.9–13.2 \times 10^{-6}$ reported for the $M = Ni$ and Fe $(La, Sr)_2MO_4$ systems [42]. For $M = Mn$ and Co, values in the range $14–16.5 \times 10^{-6}$ suggest poorer compatibility [42,50].

5. Conclusions

The solid-state reaction of $SrCeO_3$ with $LaMO_3$ and La_2NiO_4 type oxides has been evaluated in both mixed

powder and diffusion couple geometries. The results, which are anticipated to have relevance across the wider range of alkaline earth cerate and lanthanide-transition metal perovskites, clearly demonstrate that $SrCeO_3$ is non-coexistent with the perovskite phases $LaMO_3$ ($M = Mn$, Fe, Co). The reaction products in these systems, coupled with the chemical compatibility of the $La_{2-x}Sr_xNiO_4$ solid solution, indicates that appropriately doped R-P type oxides represent much better candidates for use with $SrCeO_3$. Reaction in all systems is driven by the high activity of SrO in $SrCeO_3$ and results in the formation of doped ceria as an interfacial secondary phase. This is not found to act as a diffusion barrier to Sr, suggesting that ceria should not be used to inhibit reaction in systems where a driving force exists for reaction of alkaline earth species.

Acknowledgments

The authors would like to Øystein Anderson and Trine Øyås for powder preparation. Funding for this work was provided by the NANOMAT programme; Grant No. 158517413-"Functional Oxides for Energy Technology".

References

[1] K.D. Kreuer, Annu. Rev. Mater. Res. 33 (2003) 333.
[2] T. Norby, Solid State Ionics 125 (1999) 1.
[3] H. Iwahara, Y. Asakura, K. Katahira, M. Tanaka, Solid State Ionics 168 (2004) 299.
[4] K. Sundmacher, L.K. Rihko-Struckmann, V. Galvita, Catal Today 104 (2005) 185.
[5] H. Matsumoto, T. Shimura, H. Iwahara, T. Higuchi, K. Yashiro, A. Kaimai. T. Kawada, J. Mizusaki, J. Alloy Compds. 408–412 (2006) 456.
[6] T. Schober, Solid State Ionics 162–163 (2003) 277–281.
[7] H. Iwahara, H. Uchida, K. Ono, K. Ogaki, J. Electrochem. Soc. 135 (1988) 529.
[8] H. Iwahara, Solid State Ionics 3–4 (1981) 359.
[9] N. Bonanos, K.S. Knight, B. Ellis, Solid State Ionics 79 (1995) 161.
[10] H. Iwahara, Solid State Ionics 77 (1995) 289.
[11] H. Iwahara, Solid State Ionics 86–88 (1996) 9.
[12] X.-T. Su, Q.-Z. Yan, X.-H. Ma, W.-F. Zhang, C.-C. Ge, Solid State Ionics 177 (2006) 1041.
[13] N. Maffei, L. Pelletier, A. McFarlan, J. Power Sources 136 (2004) 24.
[14] N. Sammes, R. Phillips, A. Smirnova, J. Power Sources 134 (2004) 153.
[15] S. Gopalan, A.V. Virkar, J. Electrochem. Soc. 140 (1993) 1060.
[16] S.M. Haile, G. Staneff, K.H. Ryu, J. Mater. Sci. 36 (2001) 1149.
[17] A.N. Shirsat, K.N.G. Kaimal, S.R. Bharadwaj, D.J. Das, Solid State Chem. 177 (2004) 2007.
[18] P.I. Dahl, R. Haugsrud, H. Lea Lein, T. Grande, T. Norby, M.A. Einarsrud, J. Eur. Ceram. Soc., doi:10.1016/j.jeurceramsoc.2007.03.025.
[19] G.C. Mather, F.M. Figueirdo, D.P. Fagg, T. Norby, J.R. Jurado, J.R. Frade, Solid State Ionics 158 (2003) 333.
[20] E. Boehm, A.J. McEvoy, Fuel Cells 06 (2006) 54.
[21] JCPDS-ICDD database, 1999.
[22] Bruker AXS: TOPAS V2.1: General Profile and Structure Analysis Software for Powder Diffraction Data, Bruker AXS, Karlsruhe, Germany, 2003.
[23] J.Y. Lee, J.S. Swinnea, H. Steinfink, W.M. Reiff, S. Pei, J.D. Jorgensen, J. Solid State Chem. 103 (1993) 1.
[24] F. Prado, T. Armstrong, A. Caneiro, A. Manthiram, J. Electrochem. Soc. 148 (2001) J7.
[25] A. Fossdal, M.A. Einarsrud, T. Grande, J. Am. Ceram. Soc. 88 (2005) 1988.
[26] B.C. Morris, W.R. Flavell, W.C. Mackrodt, M.A. Morris, J. Mater Chem. 3 (1993) 1007.
[27] S.V. Chavan, A.K. Tyaki, Thermochim. Acta 390 (2002) 79.
[28] R.D. Shannon, Acta Cryst. A 32 (1976) 751.
[29] T. Matsuura, J. Tabuchi, J. Mizusaki, S. Yamauchi, K. Fueki, J. Phys. Chem. Solids. 49 (1988) 1403.
[30] R.A. Mohan Ram, P. Ganguly, C.N.R. Rao, J. Solid State Chem. 70 (1987) 82.
[31] D. Senff, P. Reutler, M. Braden, O. Friedt, D. Bruns, A. Cousson, F. Bourée, M. Merz, B. Büchner, A. Revcolevschi, Phys. Rev. B. 71 (2005) 024425.
[32] P.J. Heaney, A. Mehta. G. Sarosi, V.E. Lamberti, A. Navrotsky, Phys. Rev. B. 57 (1998) 10370.
[33] A.N. Grundy, B. Hallstedt, L.J. Gauckler, CALPHAD 28 (2004) 191.
[34] L.V. Makhnach, S.P. Tolochko, V.V. Vashuk, O.V. Strukova, O.P. Ol'Shevskaya, Y.G. Zonov, Inorg. Mat. 38 (2002) 1258.
[35] S. Stølen, T. Grande, Chemical Thermodynamics of Materials: Macroscopic and Microscopic Aspects, Wiley, New York, 2004, pp. 214–215 (Chapter 7).
[36] E.H.P. Cordfunke, A.S. Booij, M.E. Huntelaar, J. Mater. Sci. 30 (1998) 437.
[37] J. Goudiakis, R.G. Haire, J. Fuger, J. Chem. Thermodyn. 22 (1990) 577.
[38] V.V. Kharton, A.A. Yaremchenko, A.L. Shaula, M.V. Patrakeev, E.N. Naumovich, D.I. Logvinovich, J.R. Frade, F.M.B. Marques, J. Solid State Chem. 177 (2004) 26.
[39] J.A. Kilner, C.K.M. Shaw, Solid State Ionics 154–155 (2002) 523.
[40] V.V. Vashook, H. Ullmann, O.P. Olshevskaya, V.P. Kulik, V.E. Lukashevich, L.V. Kokhanovskij, Solid State Ionics 138 (2000) 99.
[41] S.J. Skinner, J.A. Kilner, Solid State Ionics 135 (2000) 709.
[42] M. Al Daroukh, V.V. Vashook, H. Ullmann, F. Tietz, I. Arual Raj, Solid State Ionics 158 (2003) 141.
[43] J.W. Fergus, J. Power Sources 162 (2006) 30.
[44] G.Ch. Kostogloudis, Ch. Ftiko, A. Ahmad-Khanlou, A. Naoumidi, D. Stöver, Solid State Ionics 134 (2000) 127.
[45] K. Huang, M. Feng, J.B. Goodenough, M. Schmerling, J. Electrochem. Soc. 143 (1996) 3630.
[46] K. Wiik, C.R. Schmidt, S. Faaland, S. Shamsili, M.A. Einarsrud, T. Grande, J. Am. Ceram. Soc. 82 (1999) 721.
[47] J.R. Tolchard, T. Grande, Solid State Ionics 178 (2007) 593.
[48] S. Yamanaka, K. Kurosaki, T. Oyama, H. Muta, M. Uno, T. Matsuda, S.I. Kobayashi, J. Am. Ceram. Soc. 88 (2005) 1496.
[49] S. Yamanaka, K. Kurosaki, T. Maekawa, T. Matsuda, S. Kobayashi, U. Masayoshi, J. Nucl. Mat. 344 (2005) 61–66.
[50] C.N. Munnings, S.J. Skinner, G. Amow, P.S. Whitfield, I.J. Davidson, Solid State Ionics 177 (2006) 1849.